IEEE Access
Multidisciplinary | Rapid Review | Open Access Journal

Received November 13, 2019, accepted December 12, 2019, date of publication December 19, 2019,
date of current version December 31, 2019.

Digital Object Identifier 10.1109/ACCESS.2019.2960850

A Novel Algorithm for High-Resolution Magnetic Induction Tomography Based on Stacked Auto-Encoder for Biological Tissue Imaging

RUIJUAN CHEN[1], JUAN HUANG[1], HUIQUAN WANG[1,2], BINGNAN LI[1], ZHE ZHAO[1], JINHAI WANG[1,2], AND YAO WANG[1]

[1]School of Life Sciences, Tianjin Polytechnic University, Tianjin 300387, China
[2]Tianjin Key Laboratory of Optoelectronic Detection Technology and System, Tianjin 300387, China

Corresponding author: Yao Wang (wangyao_show@163.com)

This work was supported in part by the National Natural Science Foundation of China under Grant 61701342 and Grant 81901789, in part by the Tianjin Municipal Education Commission Scientific Research Project under Grant 2019KJ023, and in part by the Science and Technology Development Fund of Tianjin Education Commission for Higher Education under Grant 2018KJ212. All projects support young scientists and technicians to choose their own topics within the scope of NSFC funding, carry out basic research, and cultivate their ability to independently host scientific research projects and conduct innovative research.

ABSTRACT Magnetic induction tomography (MIT) is a non-invasive and non-contact imaging method that uses an excitation coil to generate time-varying magnetic fields in space and reconstruct the internal conductivity distribution based on the phase difference. In this study, a new MIT reconstruction algorithm was proposed for non-contact measurement and monitoring of the location of the anomaly in the biomedical object of interest. To reconstruct the distribution of electrical characteristics inside the biological tissue, this technique uses a stacked auto-encoder (SAE) neural network composed of a multi-layer automatic encoder. The location and reconstruction accuracy of the anomaly based on SAE and back-projection were compared, and a hemorrhagic stroke was simulated to verify the practicability of the proposed algorithm. The results showed that the relative error of reconstruction based on the SAE network algorithm reached 0.29%, which improved anomaly reconstruction accuracy and reduced the prediction time to 0.02 s. At the same time, the network was used for the reconstruction of hemorrhagic stroke in different locations, amounts, and shapes. Accordingly, the SAE neural network reconstruction algorithm proposed in this study, which can autonomously learn the non-linear relationship between input and output, can solve the defects of the traditional reconstruction algorithm, such as serious artifacts and complex calculations.

INDEX TERMS Electrical conductivity, eddy current, magnetic induction tomography, stacked auto-encoder, reconstruction algorithm.

I. INTRODUCTION

Magnetic induction tomography (MIT) is a new imaging technique based on the changes in the magnetic field caused by eddy current inside the imaging object to reconstruct the distribution of electrical conductivity [1]. This technique replaces the contact electrodes used in electrical impedance tomography (EIT) with non-contact coils. This improvement can remove the measurement error caused by contact impedance, and the magnetic field penetration force is strong, which improves the low sensitivity of EIT in the central area [2]. MIT technology has been widely used in geological exploration [3], mineral detection [4], and industrial non-destructive testing [5]. MIT is mainly applied in biomedicine field due to its strong magnetic field penetration ability, which can be applied to the detection of brain lesions or other anomaly locations [6] (such as the brain hematoma, cerebral edema, and brain tumors).

The basic principle of MIT includes both forward and inverse problems. The inverse problem of MIT is ill-posed [7], which uses the phase difference data to reconstruct conductivity distribution in the biological tissues. At present, the reconstruction algorithm of MIT can, in general, be roughly divided into linear algorithms and non-linear algorithms [8]. These algorithms include single-step schemes, such as back-projection [9], Tikhonov regularization [10], truncated singular value decomposition [11], and iterative schemes, such as the simultaneous iterative reconstruction

The associate editor coordinating the review of this manuscript and approving it for publication was Jeonghwan Gwak.

technique [11], Landweber method [12], and conjugate gradients least squares method [13]. These algorithms perform approximated linear processing on nonlinear problems, thus the reconstruction has artifacts, the error is large, and the iterative method is complicated because it requires longer duration for reconstruction. Moreover, the image resolution is not high because of the low conductivity of the biological tissues. The nonlinear algorithms include the Levenberg Marquardt method and Powell's dog-leg method [14], and these algorithms require a long calculation time and the calculation process is complex. In recent years, the MIT reconstruction algorithm has mostly been improved based on the traditional algorithm, such as the improved iterative Newton algorithm [15], Total variation function based on regularization [16], and Total variation regularization with split Bregman [17]. However, the Total variation function based on regularization is non-differentiable, and the improved Total variation function methods approach the true solution gradually through iteration. It is usually approximate, which may lead to non-optimal solution or slow convergence [17].

In this study, an algorithm based on a stacked autoencoder (SAE) neural network was proposed to reconstruct the anomaly in biological tissues. A comparison with traditional reconstruction algorithms indicated that this new method can improve the space and time resolution of anomaly location by learning the non-linear relationship between input and output data quickly and autonomously. Based on this, the feasibility of the algorithm for complex biological tissue reconstruction was verified by increasing the number of anomalies and constructing a three-layer head simulation model. Experimental results showed that by using this method, not only the electrical conductivity distribution in simple biological tissues could be reconstructed with the anomaly position located accurately, but it could also be applied to models with multi-anomalies and complex head models. Therefore, the proposed algorithm provides a new research direction for MIT and it has practical research significance for the development of MIT.

II. MAGNETIC INDUCTION TOMOGRAPHY

According to the principle of electromagnetic induction, in MIT, a sinusoidal alternating current with a certain frequency is excited into the excitation coil E, which generates a time-varying magnetic field in space, and the magnetic field is the excitation field B_m [18]. Then, the eddy current is induced in the imaging object and the disturbed magnetic field ΔB is induced to change the spatial distribution B_m [19]. The intensity of the eddy current distribution generated depends on the internal conductivity and dielectric constant distribution [20]. The intensity and distribution of the eddy current change accordingly when the conductivity distribution inside the imaging object varies, which causes the surrounding magnetic field to change, and the induced voltage and current of the detection coils also change. Thus, it is possible to reconstruct the conductivity image based on the magnetic field variation. The induced voltage obtained by the detection coils is related to the direction of the coil axis and coil parameters, and the voltage can be expressed as the surface integral of the orthogonal component of magnetic induction intensity on the coil surface [21]. That is to say, a linear relationship exists between the induced voltage and the magnetic field. Therefore, the magnetic field can be directly used to reconstruct the conductivity distribution, which provides a reference for the location and parameters optimization of the detection coil in future.

A. FORWARD PROBLEM

The forward problem in MIT is based on the Maxwell equation, which can be written as Eq. (1) [22]:

$$\begin{cases} \nabla \times \mathrm{E} + \mathrm{j}w\mu\mathrm{H} = 0 \\ \nabla \times \mathrm{H} = \mathrm{J_s} + \mathrm{J_e} \\ \nabla \cdot \mu\mathrm{H} = 0 \\ \nabla \cdot \varepsilon\mathrm{E} = 0, \end{cases} \tag{1}$$

where E is the electric intensity (V/m); $\mathrm{J_s}$ and $\mathrm{J_e}$ denote the source current density and eddy current density ($\mathrm{A/m^2}$), respectively; H is the magnetic field strength (A/m); μ and ε represent the magnetic permeability and dielectric constant in the field, respectively; and w represents the excitation angular frequency.

The relationship between the eddy current density and its electrical characteristics of the imaging object is described as Eq. (2) [23] as follows:

$$\mathrm{J_e} = (\sigma + \mathrm{j}w\varepsilon)\,\mathrm{E}. \tag{2}$$

In Eq. (2), the eddy current is composed of two parts, where the displacement current is generated by the term ε. The displacement current term in the above mentioned equation can be ignored [24] because for the biological tissue $\sigma \gg \varepsilon w$. Furthermore, the eddy current is mainly generated by the conductivity σ in the biological object, thus its magnitude is proportional to the conductivity and the excitation field frequency. By introducing the vector magnetic potential A, the differential equation of the MIT forward problem is finally obtained by using Eq. (3) as follows:

$$-\frac{1}{\mu}\nabla^2\mathrm{A} + \mathrm{j}w\sigma\mathrm{A} = \mathrm{J}. \tag{3}$$

The domain being solved is divided into multiple triangular elements, and the finite element method is used to solve the forward problem. The sum of solutions of each discrete element is approximately the solution of the entire domain [25], and thus the eddy current intensity of each partition element can be obtained as follows:

$$\mathrm{Ie} = \iint_{\Omega} (-\mathrm{j}w\sigma\mathrm{A})\,\mathrm{d}x\mathrm{d}y = -\mathrm{j}w\sigma\frac{\mathrm{A1} + \mathrm{A2} + \mathrm{A3}}{3}, \tag{4}$$

where A is the vector magnetic potential of each element; and A1, A2, and A3 are the vector magnetic potentials at the three vertices of each triangulation elements, respectively. The curl of the magnetic potential is the magnetic flux density.

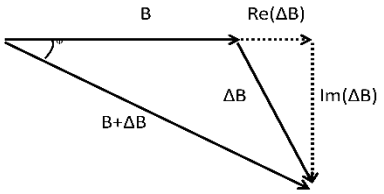

FIGURE 1. Main magnetic field and secondary magnetic field phase vector.

When the conductivity distribution is inhomogeneous, the eddy current is induced inside the imaging object, and the change in the amount of the magnetic field at the detector is calculated as follows:

$$\Delta B = \int_0^{\mathrm{R}} \mathrm{dB} = \frac{-\mathrm{jmt}\mu_0}{4\pi\sigma^2}\left[\frac{1}{4\mathrm{a}^2} - \frac{\mathrm{a}^2+2\mathrm{R}^2}{4(\mathrm{a}^2+\mathrm{R}^2)^2}\right], \quad (5)$$

where R, a, t, and m are parameters related to the model; R represents the radius of the imaging object; a represents the distance from the coil to the imaging object; t denotes the thickness of the imaging object; and m represents the parameter of excitation coil. When the skin depth is much larger than the thickness of the imaging object, then Eq. (5) can be written as follows:

$$\frac{\Delta B}{\mathrm{B}} = -\mathrm{jw}\ \sigma\ \mathrm{k} + \mathrm{w}^2\varepsilon_0\varepsilon_{\mathrm{r}}\mathrm{k}, \quad (6)$$

where σ is the internal conductivity of the imaging object, ε_{r} is the relative dielectric constant of the imaging object, ε_0 denotes the relative dielectric constant of the free space, and w is the angular frequency of the excitation signal.

Eq. (6) presents that the real part of the disturbed magnetic field ΔB is caused by the displacement current, which is related to the dielectric constant of the conductor; and the imaginary part is generated by the eddy current field, which is approximately linear with the electrical conductivity of the conductor [26]. Analysis of the phase vector diagram shows that the detected magnetic field (B+ΔB) phase lags behind the main excitation magnetic field Φ degree [26], and the phase is detected by the sensors around the imaging object. Then, the phase can be used to reconstruct the electrical impedance distribution of the object. The phase vector is shown in Fig. 1.

B. INVERSE PROBLEM

The inverse problem of MIT includes the calculation of electrical characteristic distribution of the imaging object when the magnetic field distribution around the imaging object is known [27]. Analysis of the forward problem shows that the change of phase difference is caused by the change of electrical characteristics inside the imaging object. For biological tissues, the disturbed field is weak due to the low conductivity, and $\mathrm{w}\varepsilon_0\varepsilon_{\mathrm{r}} \ll \sigma$. The imaginary part of the relative increment of the magnetic flux density, usually called SCR (phase difference), is proportional to the conductivity of the conductor [28]. If B is regarded as a reference signal, the phase difference $\Delta\Phi$ is approximately equal to the SCR, due to changes in the internal electrical properties of the tissue [29]. Therefore, Im(ΔB/B) was used as the input parameter for conductivity reconstruction and the internal conductivity distribution of the imaging object was utilized as the output parameter. The variation of the phase difference can be measured using detection coils. The results are expressed as follows:

$$\begin{cases} \Delta B = B - B_0 \\ \Delta\emptyset = Im(\frac{\Delta B}{B}), \end{cases} \quad (7)$$

where $\Delta\emptyset$ is approximately equal to the change of phase in the measuring coils [30]; and B and B_0 represent the magnetic field values measured by the coils with and without the anomaly, respectively.

The phase difference values of the different anomaly position distribution calculated by using the forward problem were used as the reconstructed data. The phase difference value was used as the input of the neural network algorithm, and the distribution of conductivity in the imaging object was used as the output. In the process, the imaging object and the anomaly were discretized into small units. The phase difference corresponding to the position of each anomaly was taken as the input of a SAE sample set, and the specific network output corresponded to the conductivity distribution of each unit. The neural network adopted the layer-by-layer greedy training method to train the sample set, that is, each training only contained a network with a hidden layer. After training the previous network, the next hidden layer was trained, and so on. Finally, the obtained training parameters were used to initialize the weight of the entire network [31].

III. STACKED AUTO-ENCODER

A. AUTO-ENCODERS

An SAE neural network is a feedback neural network model composed of multiple layer AEs [32]. Simple AE is a three-layer unsupervised learning neural network model including an input layer, a hidden layer, and an output layer [33]. The AE neural network model consists of the following two processes:

(1) The encoding process of original data x from the input layer to the hidden layer:

$$\mathrm{h} = \mathrm{g}\Theta_1(x) = \sigma(W_1 x + b_1); \quad (8)$$

(2) The decoding process from hidden layer to output layer:

$$\hat{x} = \mathrm{g}\Theta_2(x) = \sigma(W_2 x + b_2). \quad (9)$$

The AE is a neural network that reproduces the input signal as much as possible. The AE neural network model is shown in Fig. 2.

B. STACKED AUTO ENCODER

The SAE network used for this study contained two AEs and a SoftMax classifier. By using the same layer-by-layer

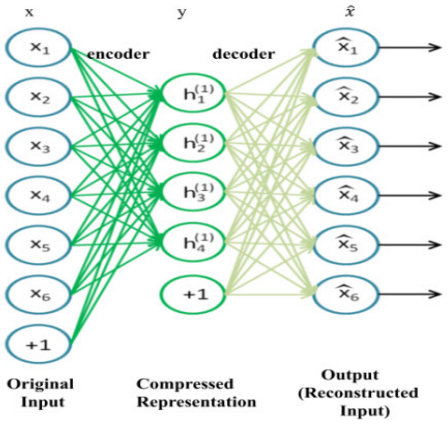

FIGURE 2. The basic structure of the automatic encoder.

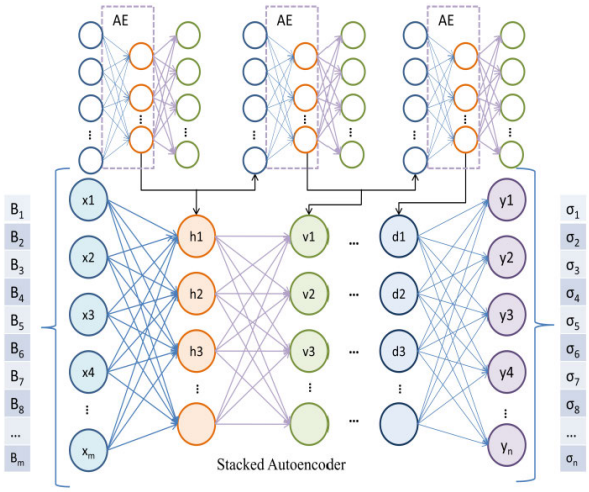

FIGURE 3. The basic structure of the SAE neural network.

greedy training method as the deep network, the input characteristics of phase difference were considered as the first layer of the neural network. The weights and bias of the first layer network were obtained as $W^{(1,1)}$, $W^{(1,2)}$, $b^{(1,1)}$, $b^{(1,2)}$. For each training sample $x^{(k)}$, the output of its hidden layer $h^{(1)(k)}$ could be obtained. The first hidden layer extracts the phase difference characteristic of the input, and then inputs the characteristic into the next hidden layer. Then, the output characteristics are encoded to train the weights and bias of the second hidden layer network $W^{(2.1)}$ and $b^{(2,2)}$, and thus the output of the second hidden layer from the encoder $h^{(2)(k)}$ can be obtained. The first-order feature of the original input is called $h^{(1)(k)}$, and the second-order feature is called $h^{(2)(k)}$ [34]. Finally, the parameters in the SAE neural network can be trained. In the process mentioned above, the ''decoding'' process of the SAE in the SAE neural network training can be discarded, and thus the second-order feature $h^{(2)(k)}$, that is, the output of the hidden layer can be directly trained as the input of the SoftMax regression [35]. The entire process is connected, as shown in Fig. 3.

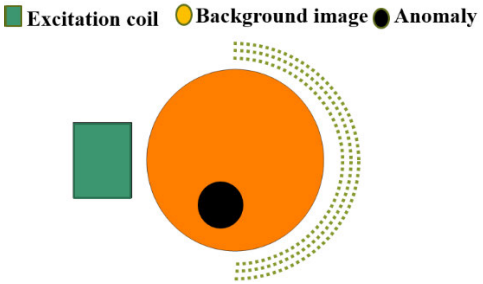

FIGURE 4. Simulation experiment model.

All the parameters required initialization, and the above mentioned process is called unsupervised pre-training. The reason why the parameters of each layer of the network are pre-trained is that the initialization of parameters is random in the previous deep network learning, which makes it difficult to train the network parameters in the lower layer, thus resulting in the phenomenon of gradient dispersion [36]. Until the parameter pre-training was proposed by Hinton in 2006, parameters of each layer of the network were initialized by self-coding. The AE mentioned in this study initializes the parameters of each layer of the network, and the training to obtain the initial value of parameters is called unsupervised parameter initialization, or ''unsupervised pre-training'' [37]. Finally, the initial network value obtained from the above mentioned pre-training is used to continue the network training to obtain the electrical conductivity distribution inside the imaging object.

IV. EXPERIMENTS

A. FORWARD PROBLEM SIMULATION MODEL

This study aims to address the imaging of biological tissue lesions, such as brain tumors, cerebral hematoma, and cerebral edema detection. Owing to the large computation amount of 3-D brain tissues, this study used a 2-D circular tissue to simulate biological tissue for forward problem analysis and to simplify the calculation (see Fig. 4). Both back-projection and SAE algorithm were used to reconstruct the conductivity distribution. The points on the opposite side in Fig. 4 are used to detect the phase difference data, and the different reconstruction methods correspond to the number and position of the different detection points. The biological tissue was a circle with a radius of 6 cm and the radius of the anomaly was 1.5 cm. The conductivity of the normal biological tissue was set to 0.25 S/m, and that of the anomaly was set to 0.05 S/m. The relative dielectric constant and relative permeability were set to 1, respectively. The height and width of the excitation coil were set to 5 and 4 cm, respectively, and the center was 9 cm away from the tissue center. In the process of simulation, an infinite element domain was added to improve the accuracy of the reconstruction data, that is, the imaging object was surrounded by an infinite air domain. Solving a problem using the finite element method requires elements segmentation of the imaging domain. The entire simulated

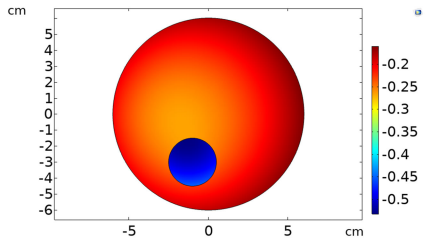

FIGURE 5. The current density of brain tissue containing brain tumor.

tissue was meshed into 9260 triangular elements, the largest of which showed a length of 2 mm.

After the model was constructed, alternating current was passed through the excitation coil, and the induced current density was calculated when the simulated model contained the anomaly as shown in Fig. 5.

B. BACK-PROJECTION RECONSTRUCTION EXPERIMENT

Sufficient reconstruction data are needed to achieve accurate position of the anomaly by the back-projection algorithm. Therefore, the excitation coil was rotated every 2° in the clockwise direction from the starting position. The phase data were detected by the 300 detection points on the opposite side of the excitation, with 100 detection points in each half-circle. The position of the detection point from the center was 8, 8.5, and 9 cm, respectively. The excitation coil was rotated 180 times and the data were back-projected to each pixel of the tissue model according to the magnetic line distribution to obtain a reconstructed image. To simplify reconstruction and avoid inverse crime, the number of units used for the inverse problem was 1442. The back-projection matrix based on magnetic lines was obtained by calculating the magnetic field at the detection points when the tissue was normal and abnormal. The sensitivity of this method to the central region and boundary regions of the tissue was different, and the projection values obtained at each pixel were averaged. Moreover, the obtained projection matrix was weighted based on the projection path and sensitivity of anomaly position.

C. STACKED AUTO-ENCODER RECONSTRUCTION EXPERIMENT

The SAE training neural network needs enough training samples to realize the anomaly location. The input data of the sample correspond to the phase difference data calculated by the forward problem, which are detected using the three half-circle magnetic field detectors placed around the imaging object. The position of the detection point is the same as that of the back-projection method. Therefore, the phase difference value of 300 around the imaging object was measured for reconstruction of the anomaly. Moreover, the number of units used for the inverse problem was 1442.

Training samples using a neural network requires sufficient sample data sets. Therefore, within the tissue simulation model, the anomaly was spread over the tissue in steps of 0.01 cm. The number of samples at 253 positions could be

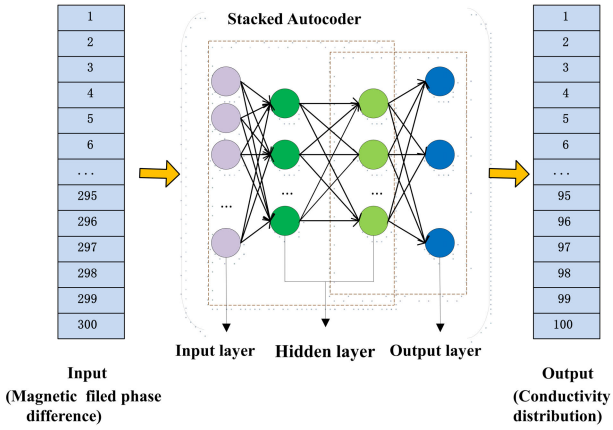

FIGURE 6. Inverse problem reconstruction neural network structure.

obtained. Three-hundred phase difference data were detected for each sample, and the 200 groups of samples were randomly selected as the input of the neural network for training, and the remaining 53 groups of samples were used as the prediction data of the neural network to evaluate the network reconstruction effect.

In the process of tissue detection and reconstruction, a four-layer network model was used for classification. The network structure was {300, 462, 712, 1442}. The input layer was the phase difference value of training samples, the middle hidden layers H1 and H2 were used to set the number of hidden layer neurons, and the output layer was the conductivity value of the 1442 units. Pre-training was performed using AE. The learning rate (LearningRate) of each layer in the training phase was set to 0.1, the number of training iterations (TrainingEpoches) was 1000, and the batch size (Batch-Size) was 10. The training network structure is shown in Fig. 6.

The process of MIT based on stacked AE algorithm is as follows:

1. Using an AE network to train the parameters from the input layer to the H1 layer. Input data form a set of vectors $X = \{x^1, x^2, \ldots, x^m,\}$ where m represents the number of training samples, and x^k (k = 1, 2, 3... m) represents the k^{th} phase difference value calculated or detected using 300 magnetic field sensors around the imaging object. After training, the decoding layer is removed, leaving only the first AE coding stage.

2. Train the parameters from H1 to H2. The activation value of the H1 layer is used as the input of the H2 layer and continues to train the second encoder.

3. Connect the output of the second layer to the classification layer SoftMax for multi-classification tasks. The classification label obtained by the classification is the training output. The data output of the neural network algorithm is a set of vectors $O = \{o^1, o^2, \ldots, o^m\}$, where m represents the number of training samples, and o^k (k = 1, 2, 3... m) represents the conductivity of 1442 independent subdivision units. The data structure used for imaging quality testing is the same as the training data.

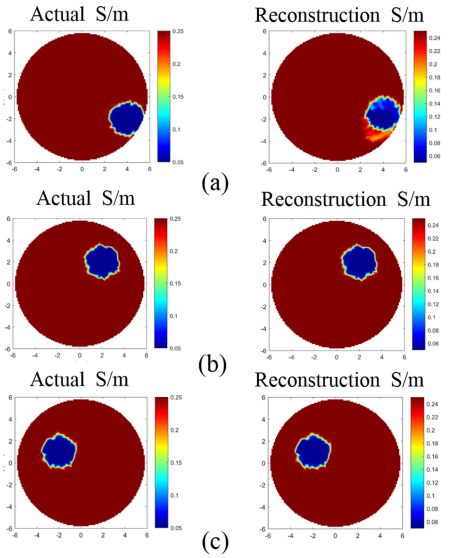

FIGURE 7. SAE neural network for anomaly reconstruction results.

4. After the network training, the imaging quality is tested with randomly assigned testing sample sets, and the reconstructed conductivity distribution is visualized, compared, and calculated with the preset conductivity distribution, and the reconstruction error is obtained.

V. RESULTS AND ANALYSIS

A. STACKED AUTO-ENCODER RECONSTRUCTION RESULTS

A network for biological lesion detection was obtained by training the SAE neural network model. 53 groups of phase difference data samples used for testing were brought into the network for prediction, and the reconstruction results are shown in Fig. 7. The left side of Fig. 7 shows the actual conductivity distribution of the tissue model with an anomaly while the right side is the conductivity distribution predicted by the SAE neural network proposed in this study.

According to the prediction results of the three groups, the SAE network can be used to reconstruct the location of the anomaly well and greatly improve the reconstruction artifacts. Moreover, the network can well predict the boundary and regional center of biological tissue.

B. COMPARISON OF STACKED AUTO-ENCODER AND BACK-PROJECTION RECONSTRUCTION

To evaluate the feasibility of the reconstruction method for anomaly location and monitoring proposed in this study, the anomaly of the same position inside the tissue was selected and the predicted results of the SAE network were compared with the back-projection results. The comparison results are shown in Fig. 8. The true conductivity distribution of the anomaly is shown in Fig. 8 (a), the conductivity distribution predicted by the trained SAE neural network is shown in Fig. 8(b), and the conductivity distribution reconstructed by the back-projection algorithm is presented in Fig. 8(c).

According to the reconstruction results, compared to the back-projection algorithm, the SAE neural network proposed

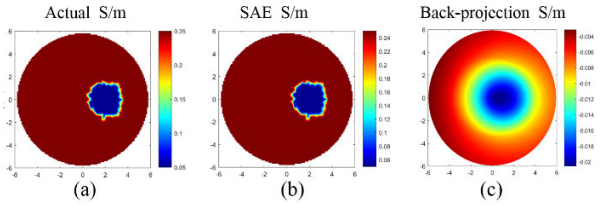

FIGURE 8. Comparison between SAE neural network and back-projection algorithm for abnormal reconstruction.

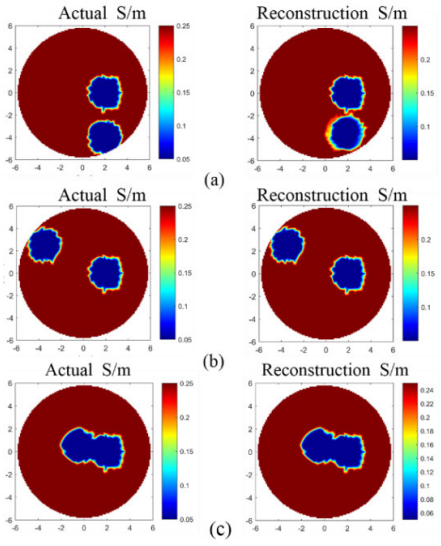

FIGURE 9. SAE neural network reconstruction results for multiple anomalies.

here is more accurate with respect to the positioning and conductivity values of the anomaly, and the reconstruction error is smaller, which significantly improves the artifacts. Moreover, it has a short prediction time of 0.02 s, which can realize the requirements of rapid positioning.

C. STACKED AUTO-ENCODER RECONSTRUCTION RESULTS OF MULTIPLE ANOMALIES

To verify the feasibility of the SAE neural network for multiple anomaly reconstruction, based on an anomaly reconstruction, this study included an equal-sized anomaly to the tissue to simulate multiple lesions. The model constructed 153 multiple anomalies samples, among which 100 were randomly selected as training samples and 53 as prediction samples. The training process was similar to the single anomaly, and the reconstruction result is shown in Fig. 9. The SAE neural network can also realize the localization and detection of multiple anomalies, and its anomalies shape and size are clearly visible. Fig. 9 presents the result when the distance between the two anomalies decreases until contact.

D. STACKED AUTO-ENCODER RECONSTRUCTION RESULTS OF A COMPLEX BRAIN MODEL

To evaluate the feasibility of the SAE neural networks for complex tissue reconstruction, a simplified three-layer model

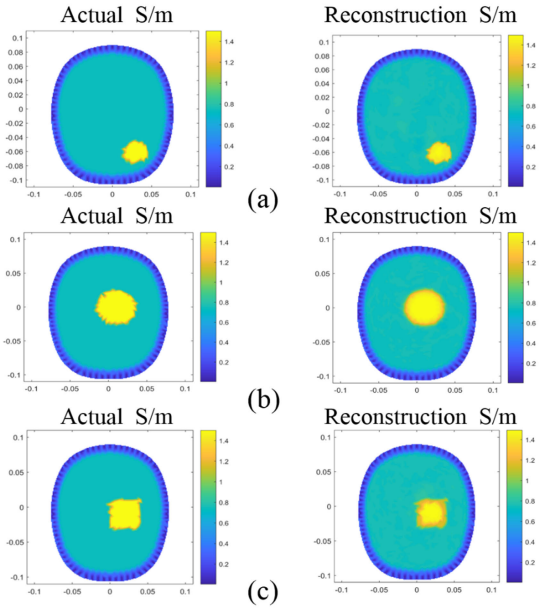

FIGURE 10. Reconstruction results of the simulated three-layer head by SAE neural network.

was developed to simulate a hemorrhagic stroke, which included the cerebral cortex, skull, and scalp from the inside to the outside. The ratio of each part of the simulated brain tissue was 0.87:0.92:1 and the tissues were set to be isotropic. Electrical conductivity numerical simulation parameters were set as follows: electrical conductivity of the cerebral cortex was 0.75 S / m, that of the skull was 0.0042 S / m, and that of the scalp was 0.33 S / m. Studies have shown that the electrical conductivity of hemorrhagic tissues at a high frequency (> 100 KHZ) can be twice as high as that of normal brain tissues [38], and thus the simulated conductivity of hemorrhagic tissue was set to 1.5 S / m. Comsol software was used to segment the established model.

The network was trained with samples of different locations, different amounts of bleeding (that is, different volumes) and square bleeding shapes, thus increasing the variety of samples and enabling it to reconstruct bleeding in different locations, amounts of bleeding, and different shapes. The number of samples in the three forms was 308, among which 280 were randomly selected as training samples and the remaining 28 as prediction samples. The network structure was {300, 570, 1080, 1566}. The training times were set to 10 and the training time was about 1.5 h (the processor of the computer was Intel(R) Core (TM) i7-5500U CPU @ 2.40GHz and the system type was 64-bit with 8 GB of memory). If the CPU performance is better, the time is shortened. Then, the prediction samples were input into the established network, and the predicted results of different positions, different bleeding volumes, and different bleeding shapes are shown in Fig. 10. The left side of the figure is the real conductivity distribution, and the right side is the reconstructed conductivity distribution by the SAE neural network. The reconstruction results showed that the prediction of bleeding location, bleeding volume, and bleeding shape were correct without obvious artifact.

TABLE 1. SAE neural network and back-projection reconstruction results.

	RMSE(x, h)	MAE(x, h)	d_A	R
Back-projection	64.73%	28.16%	29.98%	36.33%
SAE	0.06%	0.01%	0.06%	0.25%

E. ANALYSIS OF RECONSTRUCTION RESULTS

To evaluate the accuracy of the SAE reconstruction algorithm for anomaly localization, in this study quantitative analysis of the reconstruction results was carried out by calculating the root mean square error (RMSE), mean absolute error (MAE), normalized mean square error (NMAD), and reconstruction relative error (RE) of the reconstructed image. The calculation principle of each part is described thoroughly. The reconstruction results calculated by different reconstruction methods for the same anomaly position are summarized in Table 1.

1) RMSE

The sum of the square of the deviation between the reconstructed value, the true value, and the square root of the ratio of the total conductivity of the reconstructed sample m, which is used to measure the deviation between the reconstructed conductivity value and the true value. The RMSE is calculated as follows:

$$\mathrm{RMSE}\,(\mathrm{x},\mathrm{h}) = \sqrt{\frac{1}{m}\sum_{i=1}^{m}(h(x^{(i)}) - y^{(i)})^2}, \tag{10}$$

where $\mathrm{h}(\mathrm{x}^{(\mathrm{i})})$ is the reconstructed conductivity value, $\mathrm{y}^{(\mathrm{i})})$ is the conductivity true value, and m denotes the total conductivity number of each sample used to reconstruct the image.

2) MAE

The average value of the absolute error, which is used to reflect the actual situation of the reconstructed value error. The MAE is calculated as follows:

$$\mathrm{MAE}\,(\mathrm{x},\mathrm{h}) = \frac{1}{\mathrm{m}}\sum_{\mathrm{i}=1}^{\mathrm{m}}|\mathrm{h}(\mathrm{x}^{(\mathrm{i})}) - \mathrm{y}^{(\mathrm{i})}|. \tag{11}$$

3) NMAD

When $\mathrm{d_A} = 0$, the reconstructed image has no difference from the actual image. The larger the $\mathrm{d_A}$, the larger the error between the reconstructed image and the actual image. The NMAD is calculated as follows:

$$\mathrm{d_A} = \frac{\sum_{\mathrm{i}=1}^{\mathrm{m}}(|\sigma_{\mathrm{mi}} - \sigma_{\mathrm{si}}|)}{\sum_{\mathrm{i}=1}^{\mathrm{m}}(|\sigma_{\mathrm{mi}}|)}, \tag{12}$$

where m represents the number of conductivities reconstructed under each sample, σ_{mi} is the true conductivity value, and σ_{si} denotes the reconstructed conductivity value.

TABLE 2. The Average results of test samples for all models reconstructed using SAE.

	RMSE(x, h)	MAE(x, h)	d_A	R
Single anomaly	0.07%	0.02%	0.08%	0.29%
multi-anomaly	2.27%	0.51%	2.23%	9.62%
complex three-layer head	0.92%	0.40%	0.65%	1.35%

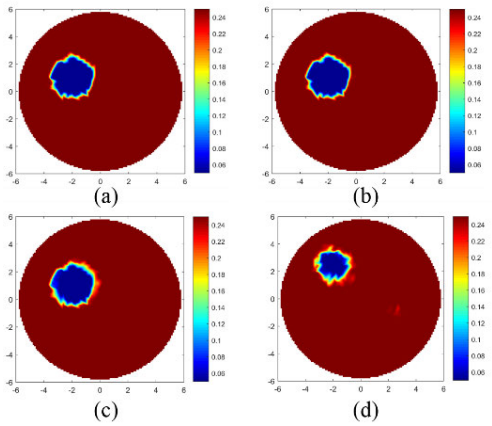

FIGURE 11. Reconstruction results of a single anomaly under different noises.

TABLE 3. The single anomaly reconstruction results after adding different degrees of noise.

	RMSE(x, h)	MAE(x, h)	d_A	R
80dB	0.07%	0.02%	0.08%	0.29%
60dB	0.07%	0.02%	0.08%	0.29%
40dB	0.18%	0.03%	0.14%	0.76%
20dB	3.18%	0.57%	2.42%	13.12%

4) RE

The relative error of reconstruction is calculated by using the binary norm of the difference between the real conductivity and the reconstructed conductivity. The RE is calculated as follows:

$$\mathrm{R} = \frac{\|\sigma_{\mathrm{Reconstruction}} - \sigma_{\mathrm{Actual}}\|}{\|\sigma_{\mathrm{Actual}}\|} \times 100\%, \tag{13}$$

where $\sigma_{\mathrm{Reconstruction}}$ represents the reconstructed conductivity vector and $\sigma_{\mathrm{Actural}}$ represents the true conductivity vector.

For the quantitative calculation of an anomaly, multi-anomaly, and complex three-layer head model, the average value of the predicted conductivity distribution results of all test samples was calculated in this study, and the results are presented in Table 2.

F. STACKED AUTO-ENCODER NOISE RESISTANCE ANALYSIS

Different degrees of noise were added in the data to analyze the anti-noise performance of the SAE neural network proposed in this study. The reconstruction results with noises of 80, 60, 40, and 20 dB added into the simulated single abnormal biological tissue model, multiple abnormal biological tissue model, and three-layer head model are shown in Figs. 11 – 13, respectively. Clearly, the SAE neural network

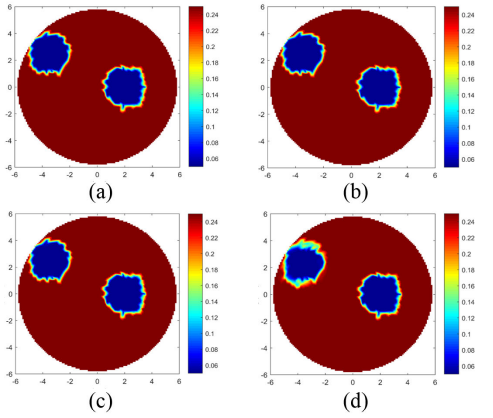

FIGURE 12. Reconstruction results of multiple anomalies under different noises.

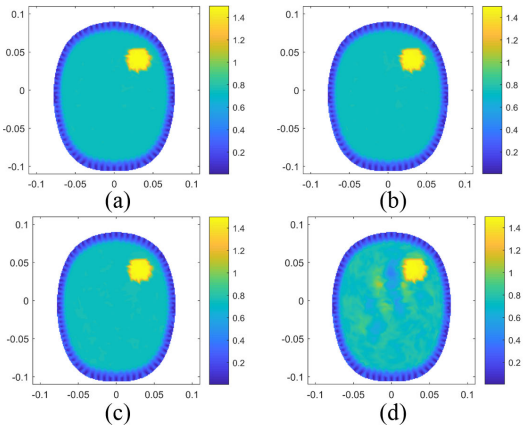

FIGURE 13. Reconstruction results of the three-layer head under different noises.

TABLE 4. The multi-anomaly reconstruction results after adding different degrees of noise.

	RMSE(x, h)	MAE(x, h)	d_A	R
80dB	2.27%	0.50%	2.22%	9.61%
60dB	2.27%	0.50%	2.22%	9.63%
40dB	2.32%	0.53%	2.33%	9.84%
20dB	2.73%	0.67%	2.97%	11.57%

TABLE 5. The complex three-layer head reconstruction results after adding different degrees of noise.

	RMSE(x, h)	MAE(x, h)	d_A	R
80dB	0.92%	0.40%	0.65%	1.35%
60dB	0.94%	0.42%	0.69%	1.38%
40dB	1.03%	0.5%	0.82%	1.52%
20dB	9.22%	4.82%	7.87%	13.62%

can still reconstruct the location and size of the anomaly after adding noise. In the reconstruction results after adding 20dB noise, there was a small artifact in the brain background but it did not affect the positioning accuracy. When 80, 60, and 40 dB of noise were added, the anti-noise performance of the network was excellent. The error calculation results for the different models are presented in Tables 3 – 5.

VI. CONCLUSION

In this study, a fast reconstruction method for brain disease detection based on SAE neural network was proposed. The superiority of the algorithm was verified through comparison with the magnetic field line back-projection algorithm. Furthermore, compared with the current popular iterative algorithms based on improved traditional algorithms, the proposed algorithm can learn the nonlinear relationship between the input and output data autonomously and systematically. Moreover, the network complexity is low, the calculation process is simplified, and the network prediction results are highly accurate and fast, showing great advantages in rapid and accurate reconstruction. This method can be applied to clinical continuous monitoring and diagnosis of diseases.

REFERENCES

[1] M. Dai, T. Sun, X. Chen, L. Yu, M. Chen, P. Hao, X. Zeng, J. Yan, and S. Chen, "A B-scan imaging method of conductivity variation detection for magneto–acousto–electrical tomography," *IEEE Access*, vol. 7, pp. 26881–26891, 2019.

[2] L. Wang, R.-G. Liu, W. Zhou, and X.-Z. Dong, "Research progress of magnetic induction tomography system and experimental results," *Chin. Med. Equip. J.*, vol. 34, no. 2, pp. 85–88, 2013.

[3] Z. Zakaria, M. S. B. Mansor, and R. A. Rahim, "Magnetic induction tomography: A review on the potential application in agricultural industry of Malaysia," *J. Agricult. Sci.*, vol. 5, no. 9, pp. 78–82, 2013.

[4] C. von Hebel, S. Rudolph, A. Mester, J. A. Huisman, P. Kumbhar, H. Vereecken, and J. van der Kruk, "Three-dimensional imaging of subsurface structural patterns using quantitative large-scale multiconfiguration electromagnetic induction data," *Water Resour. Res.*, vol. 50, no. 3, pp. 2732–2748, 2014.

[5] P. Bevington, R. Gartman, and W. Chalupczak, "Non-destructive structural imaging of steelwork with atomic magnetometers," *Appl. Phys. Lett.*, vol. 113, no. 6, 2018, Art. no. 063503.

[6] Y. D. Jiang and M. Soleimani, "Capacitively coupled resistivity imaging for biomaterial and biomedical applications," *IEEE Access*, vol. 6, pp. 27069–27079, 2018.

[7] C. Ktistis, D. W. Armitage, and A. J. Peyton, "Calculation of the forward problem for absolute image reconstruction in MIT," *Physiol. Meas.*, vol. 29, no. 6, pp. S455–S464, 2008.

[8] R. Merwa, K. Hollaus, P. Brunner, and H. Scharfetter, "Solution of the inverse problem of magnetic induction tomography (MIT)," *Physiol. Meas.*, vol. 26, no. 2, p. 241, 2005.

[9] L. Ke, F. Cao, and Q. Du, "Back-projection matrix calculation and data processing methods used in magnetic induction tomography," *Chin. J. Sci. Instrum.*, vol. 35, no. 10, pp. 2256–2262, 2014.

[10] H. Wei and M. Soleimani, "Four dimensional reconstruction using magnetic induction tomography: Experimental study," *Prog. Electromagn. Res.*, vol. 129, pp. 17–32, Jan. 2012.

[11] J. Shi, X. Cao, and F. Liu, "Greedy reconstruction algorithm for fluorescence molecular tomography by means of truncated singular value decomposition conversion," *J. Opt. Soc. Amer. A, Opt. Image Sci.*, vol. 30, no. 3, pp. 47–437, 2013.

[12] H. Wei and M. Soleimani, "Volumetric magnetic induction tomography," *Meas. Sci. Technol.*, vol. 23, no. 4, 2012, Art. no. 055401.

[13] H. Wei and M. Soleimani, "Three-dimensional magnetic induction tomography imaging using a matrix free Krylov subspace inversion algorithm," *Prog. Electromagn. Res.*, vol. 122, pp. 29–45, Jan. 2012.

[14] M. Soleimani and B. Lionheart, "Absolute conductivity reconstruction in magnetic induction tomography using a nonlinear method," *IEEE Trans. Med. Imag.*, vol. 25, no. 12, pp. 1521–1530, Dec. 2006.

[15] M. Han, Y. Xue, and P. Qin, "An improved image reconstruction algorithm based on iteration NR in magnetic induction tomography," *Chin. J. Biomed. Eng.*, vol. 34, no. 2, pp. 190–197, Apr. 2016.

[16] Y. Chen, W. Xu, and L. Yi, "A image reconstruction algorithm based on variation regularization for magnetic induction tomography," in *Proc. Cross Strait Quad-Regional Radio Sci. Wireless Technol. Conf.*, 2011.

[17] F. Li, J. F. P. J. Abascal, M. Desco, and M. Soleimani, "Total variation regularization with split Bregman-based method in magnetic induction tomography using experimental data," *IEEE Sensors J.*, vol. 17, no. 4, pp. 976–985, Feb. 2017.

[18] Y. Li, D. Xiuzhen, and L. Ruigang, "Fundamental study on sensitivity of medical magnetic inductive impedance imaging," *Chin. Med. Equip. J.*, pp. 1–2, Mar. 2006.

[19] Y. Saeys, I. Inza, and P. Larranaga, "A review of feature selection techniques in bioinformatics," *Bioinformatics*, vol. 23, no. 19, pp. 2507–2517, 2007.

[20] Z. Xiao, C. Tan, and F. Dong, "Multi-frequency difference method for intracranial hemorrhage detection by magnetic induction tomography," *Physiol. Meas.*, vol. 39, no. 5, 2018, Art. no. 055006.

[21] M. Dai, X. Chen, M. Chen, H. Lin, F. Li, and S. Chen, "A novel method to detect interface of conductivity changes in magneto-acousto-electrical tomography using chirp signal excitation method," *IEEE Access*, vol. 6, pp. 33503–33512, 2018.

[22] D. Gürsoy and H. Scharfetter, "The effect of receiver coil orientations on the imaging performance of magnetic induction tomography," *Meas. Sci. Technol.*, vol. 20, no. 10, 2009, Art. no. 105505.

[23] C. Tan, Y. Wu, Z. Xiao, and F. Dong, "Optimization of dual frequency-difference MIT sensor array based on sensitivity and resolution analysis," *IEEE Access*, vol. 6, pp. 34911–34920, 2018.

[24] L. Zhang, P. Tian, X. Jin, and W. Tong, "Numerical simulation of forward problem for electrical capacitance tomography using element-free Galerkin method," *Eng. Anal. Boundary Elements*, vol. 34, pp. 477–482, May 2010.

[25] H. Scharfetter, "Feasibility of lung imaging using magnetic induction tomography," in *Proc. World Congr. Med. Phys. Biomed. Eng.*, in IFMBE Proceedings. Berlin, Germany: Springer, vol. 25, 2009, pp. 525–528.

[26] M. H. Pham and A. J. Peyton, "A model for the forward problem in magnetic induction tomography using boundary integral equations," *IEEE Trans. Magn.*, vol. 44, no. 10, pp. 2262–2267, Oct. 2008.

[27] P. Wencai, Y. Qingguang, and Q. Mingxin, "Detection of cerebral hemorrhage in rabbits by time-difference magnetic inductive phase shift spectroscopy," *PLoS ONE*, vol. 10, no. 5, 2015, Art. no. 128127.

[28] B. Dekdouk, "Image reconstruction of low conductivity material distribution using magnetic induction tomography," *Data Archit.*, vol. 28, pp. 139–155, 2011.

[29] P. Brunner, R. Merwa, A. Missner, J. Rosell, K. Hollaus, and H. Scharfetter, "Reconstruction of the shape of conductivity spectra using differential multi-frequency magnetic induction tomography," *Physiolog. Meas.*, vol. 27, no. 5, p. S237, 2006.

[30] R. Palka, S. Gratkowski, and K. Stawicki, "The forward and inverse problems in magnetic induction tomography of low conductivity structures," *Eng. Comput.*, vol. 26, no. 7, pp. 843–856, 2009.

[31] R. Merwa, K. Hollaus, P. Brunner, and H. Scharfetter, "Solution of the inverse problem of magnetic induction tomography (MIT)," *Physiol. Meas.*, vol. 26, no. 2, p. 241, 2005.

[32] S. Martin and C. T. M. Choi, "Nonlinear electrical impedance tomography reconstruction using artificial neural networks and particle swarm optimization," *IEEE Trans. Magn.*, vol. 52, no. 3, pp. 1–4, Mar. 2016.

[33] X. Li, L. Peng, Y. Hu, J. Shao, and T. Chi, "Deep learning architecture for air quality predictions," *Environ. Sci. Pollut. Res.*, vol. 23, no. 22, pp. 22408–22417, 2016.

[34] M. Germain, K. Gregor, and I. Murray, "MADE: Masked autoencoder for distribution estimation," in *Proc. Int. Conf. Mach. Learn.*, 2015, pp. 881–889.

[35] V. L. Cao, M. Nicolau, and J. Mcdermott, "A hybrid autoencoder and density estimation model for anomaly detection," in *Parallel Problem Solving from Nature*. Edinburgh, U.K.: Springer, Sep. 2016.

[36] H. Badem, A. Caliskan, and A. Basturk, "Classification of human activity by using a stacked auto-encoder," in *Proc. Med. Technol. Nat. Congr. (TIPTEKNO)*, Oct. 2016, pp. 1–4.

[37] E. P. Ijjina and K. Mohan, "Classification of human actions using pose-based features and stacked auto encoder," *Pattern Recognit. Lett.*, vol. 87, no. 2, pp. 268–277, Nov. 2016.
[38] W. Xiaoming and D. Xiuzhen, "Complex impedance frequency response of human brain tissues and its equivalent circuit model," *Chin. J. Clin. Rehabil.*, vol. 17, no. 3, pp. 589–602, 2005.

RUIJUAN CHEN was born in 1984. She received the B.Sc. degree from the School of Physical Science and Technology, Hebei University, in 2006, the M.Sc. degree from the Hebei University of Technology, in 2009, and the Ph.D. degree from Tianjin University, in 2012.

From 2012 to 2014, she was with the National Center for Microscopic Imaging, University of California, San Diego. She is currently a M.Sc. Supervisor with the School of Electronics and Information Engineering, Tianjin Polytechnic University. Her main research interests include biomedical imaging, biomedical image processing, and biomedical information detection.

JUAN HUANG was born in 1995. She received the bachelor's degree in electronics and information engineering from Xinyang Normal University, in 2018. She is currently pursuing the master's degree in electronics and information engineering with Tianjin Polytechnic University.

Her current research interest includes biomedical imaging.

HUIQUAN WANG was born in 1985. He received the bachelor's and Ph.D. degrees in biomedical engineering from the School of Precision Instruments and Optoelectronics Engineering, Tianjin University, the bachelor's degree in international finance from Nankai University, and the Ph.D. degree in instrument science and technology from Tianjin University.

From 2011 to 2013, he was a Public Visiting Scholars study with Johns Hopkins University. He is currently the Director of the Department of Biomedical Engineering and the Master Instructor of Tianjin Polytechnic University. His main research interests include wearable medical testing equipment and intervention methods, near-infrared spectroscopy and big data mining algorithms, and multimodal imaging technology.

BINGNAN LI was born in 1995. He received the bachelor's degree in communication engineering from Tiangong University, in 2017, where he is currently pursuing the master's degree in biomedical engineering.

His main research interests include biomedical imaging, magnetic induction tomography, and magnetic detection electrical impedance tomography.

ZHE ZHAO received the bachelor's, master's, and Ph.D. degrees in biomedical engineering from the School of Precision Instruments and Optoelectronics Engineering, Tianjin University.

In 2012, she was a National Scholar with the BME Department, Johns Hopkins University, for a one-year visit. She was a Lecturer with Tianjin Polytechnic University, focusing on hyperspectral analysis and complex solution composition analysis.

JINHAI WANG was born in 1966. He received the bachelor's degree in automatic control from the Department of Information and Control Engineering, Xi'an Jiaotong University, in 1987, the master's degree in computer application technology from the Department of Automation, Tianjin Polytechnic University, in 1999, and the Ph.D. degree in physical electronics from the School of Precision Instrument and Optoelectronics Engineering, Tianjin University, in 2007.

In 2005, he became a Senior Honorary Researcher at the University of Auckland, New Zealand, and a Visiting Scholar of electronics and computer science. He is currently the Dean of the School of Electronics and Information Engineering, Tianjin Polytechnic University, the Branch Executive of the National Computer Institute of Tianjin MCU, a member of higher education working committee in Tianjin communication association, the Director of the Tianjin Institute of Biomedical Engineering, and the Organizing Committee member and the Panel member of National Electronic Design Competition of Tianjin Division.

YAO WANG was born in 1988. She received the bachelor's degree in biomedical engineering from the Department of Biological Sciences and Engineering, South China University of Technology, in 2011, and the Ph.D. degree in biomedical engineering from the Department of Medicine, Tsinghua University, in 2016.

Since 2016, she has been a Lecturer with Tianjin Polytechnic University. Her main research interests include auditory signal processing and detection, brain-computer interface research based on auditory signals, and auditory and cognitive engineering research.